Vascular-targeted micelles as a specific MRI contrast agent for molecular imaging of fibrin clots and cancer cells

Vassily Vorobiev [a,b], Souad Adriouach [a,b], Lindsey A. Crowe [c], Sébastien Lenglet [d], Aurélien Thomas [e,f], Anne-Sophie Chauvin [g], Eric Allémann [a,b,*]

[a] *School of Pharmaceutical Sciences, University of Geneva, 1211 Geneva, Switzerland*
[b] *Institute of Pharmaceutical Sciences of Western Switzerland, University of Geneva, 1211 Geneva, Switzerland*
[c] *Department of Radiology and Medical Informatics, University of Geneva, 1211 Geneva, Switzerland*
[d] *Forensic Toxicology and Chemistry Unit, University Center for Legal Medicine, Geneva University Hospital, 1211 Geneva, Switzerland*
[e] *Unit of Toxicology, CURML, Lausanne University Hospital, Geneva University Hospitals, Switzerland*
[f] *Faculty of Biology and Medicine, University of Lausanne, 1015 Lausanne, Switzerland*
[g] *Institut of Chemical Sciences and Engineering, Swiss Federal Institute of Technology of Lausanne, Route Cantonale, 1015 Lausanne, Switzerland*

ARTICLE INFO

ABSTRACT

Molecular medical imaging is intended to increase the accuracy of diagnosis, particularly in cardiovascular and cancer-related diseases, where early detection could significantly increase the treatment success rate. In this study, we present mixed micelles formed from four building blocks as a magnetic resonance imaging targeted contrast agent for the detection of atheroma and cancer cells. The building blocks are a gadolinium-loaded DOTA ring responsible for contrast enhancement, a fibrin-specific CREKA pentapeptide responsible for targeting, a fluorescent dye and DSPE-PEG$_{2000}$. The micelles were fully characterized in terms of their size, zeta potential, stability, relaxivity and toxicity. Target binding assays performed on fibrin clots were quantified by fluorescence and image signal intensities and proved the binding power. An additional internalization assay showed that the micelles were also designed to specifically enter into cancer cells. Overall, these multimodal mixed micelles represent a potential formulation for MRI molecular imaging of atheroma and cancer cells.

1. Introduction

Cardiovascular disease and cancer are the primary causes of human death worldwide [1]. Early diagnosis therefore plays a key role in the successful treatment and increased survival rate of both diseases. Medical imaging techniques such as magnetic resonance imaging (MRI), computed tomography, positron emission tomography or ultrasound are commonly used for the detection and diagnosis of these diseases.

To further improve the diagnostic quality and interpretability of the images, continuous improvements are made on devices and software, on one hand [2], and, on the other hand, research towards the synthesis of new target-specific contrast agents (CAs) and tracers for molecular imaging is conducted [3,4].

MRI is a noninvasive diagnostic procedure that allows imaging of all parts of the human body, especially soft tissues [5]. To overcome the low sensitivity of the technique and to highlight different tissues that would normally have the same contrast, gadolinium (Gd)-based contrast agents (Gd-CA), in which the Gd(III) cation is strongly chelated, are commonly injected during MRI scans. They affect the signal by shortening the T1-relaxivity time of the proton and thus positively enhance the contrast in the tissues where they are located. They are indirect CAs, as they are not directly observed on the final image, contrary to contrast agents used in other imaging modalities [6]. Research on direct MRI CAs has been undertaken but has not yet led to commercial products [7].

Gd-CAs can be classified in several ways. First, the structure of the chelate can be considered: 1,4,7,10-tetraazacyclododecane-1,4,7,10-tetraacetic acid (DOTA) is a macrocyclic ligand with the advantage of being extremely stable with no Gd release [8], whereas the linear diethylentriaminepenta-acetic acid (DTPA) ligand [9] forms less stable complexes. For more than ten years, Gd-DTPA has been associated with severe side effects due to the propensity of Gd^{3+} release from DTPA. This may lead to nephrogenic systemic fibrosis (NSF) [10] or Gd brain

deposition [11]. Second, Gd-CAs can be classified according to the fate of the molecule in the body. On the one hand, Gd-DOTA and Gd-DTPA are called extravascular CAs because of their fast clearance after injection, mostly by kidneys and partly by the liver [12]. Fortunately, a fraction of the injected dose escapes the vessels and diffuses for a short period of time in the tissues of interest, such as brain structures, hematomas, tumors, joints and others [6]. On the other hand, blood pool contrast agents (BPCAs), such as Gadofosveset [13] and Gd-micelles [14,15], remain in the vascular compartment longer and allow imaging of the cardiovascular system even with long MRI sequences [16].

Finally, as mentioned above, research is now focused on target-specific CAs, which will accumulate mainly in a selected tissue [17] or a specific cellular target [18], allowing molecular imaging, which is crucial for early and precise diagnosis.

Above all, MRI CA development faces another issue: new high-magnetic-field MRI equipment significantly decreases the relaxivity potential of Gd-CAs, requiring the introduction of a higher concentration of product to increase the signal [19,20]. The property relaxivity is therefore a crucial parameter in Gd-CA development.

Currently, there is an increased need for high-relaxivity vascular-

Table 1
Building blocks and their roles.

Building block		Role	Chemical structure
1	Gd-DO3A-Tyr-(C$_{18}$)$_2$	Gd-CA	
2	DSPE-PEG$_{2000}$-CREKA	Fibrin binding block	
2$_{bis}$	DSPE-PEG$_{2000}$-CERAK	Fibrin nonbinding control	
3	DSPE-PEG$_{2000}$-IR-774	Fluorescent block	
4	DSPE-PEG$_{2000}$	Stabilizing block	

Building blocks :

Gd-DO3A-Tyr-(C$_{18}$)$_2$ DSPE-PEG$_{2000}$-CREKA   DSPE-PEG$_{2000}$-IR-774   DSPE-PEG$_{2000}$
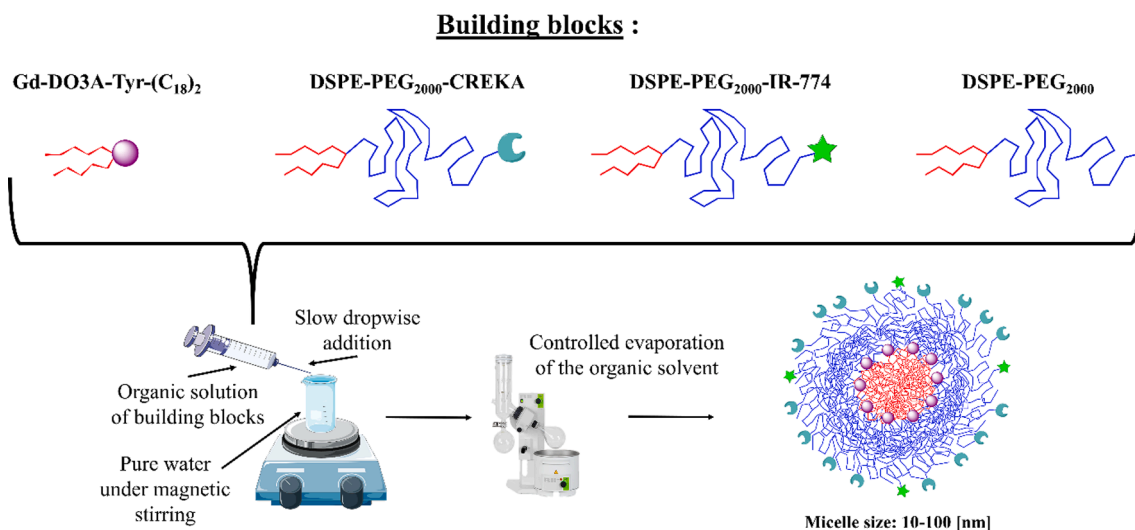
Fig. 1. Mixed micelle formulation by nanoprecipitation.

targeted specific BPCAs that will enable molecular imaging for an early diagnosis of vascular disease and vascularized tumor tissues. One approach is to design supramolecular nanoconstructs having a size that impedes excessively fast tissue diffusion and clearance. These materials incorporate imaging moieties and targeting moieties and potentially an additional drug for theranostic purposes. Such nanoconstructs may be nanoparticles, liposomes or micelles [15,21–23]. To date, several peptides and antibodies have been added to MRI supramolecular constructs [24–27]. Among others, the Cys-Arg-Glu-Lys-Ala peptide (CREKA) showed very encouraging results as a targeting moiety for blood clots [18,28]. This pentapeptide binds specifically to fibrin clots that are formed during blood coagulation [29]. This can occur either on the surface of atheroma plaques or in small leaky vessels of tumors. It is therefore a peptide of interest to be incorporated into the structure of supramolecular Gd-CAs for molecular imaging.

Previously, we reported several micelle formulations designed as BPCA for MRI [14,15,30,31]. They circulated for a prolonged period of time in blood vessels and allowed cardiovascular imaging with high resolution. The results obtained in our previous MRI studies led us to add a targeting moiety on supramolecular nanoconstructs for molecular imaging.

Therefore, the aim of the present work was to develop a BPCA for MRI of atherosclerosis. Here, we report the synthesis of building blocks and formulation of a novel mixed-micelle for vascular targeting. Three building blocks were synthesized:

(1) Gd-DO3A-Tyr-$(C_{18})_2$ for MRI imaging [32], (2) DSPE-PEG$_{2000}$-CREKA for targeting and (3) DSPE-PEG$_{2000}$-IR-774 for orthogonal fluorescence detection and potential cancer cell internalization. DSPE-PEG$_{2000}$ was added for the stabilization of the micelles [33]. Three different micelle compositions, varying in proportion of the targeting moiety, were tested. The micelles were characterized in terms of their size, zeta potential, stability and relaxivity properties. Four different cell lines were chosen for *in vitro* cytotoxicity evaluation and fluorescence imaging. The efficiency of MRI was determined by scans on phantoms. Finally, fibrin clot binding assays were performed *in vitro* with either fluorescence detection or MRI.

This research provides an improved way for imaging and diagnosis of atherosclerosis and cancer cells detection, the two leading causes of human death. Results and findings of this study show the significance advancement towards targeted vascular MRI contrast agents.

2. Materials and methods

2.1. Synthesis of micelle building blocks

Building blocks were synthesized according to published procedures [14,15,34–36].

The synthetic details and Gd^{3+} loading of the chelates are reported in the Supplementary Information. The micelles were formulated with four building blocks (Table 1). DSPE-PEG$_{2000}$ was purchased from Sigma-Aldrich (Buchs, Switzerland), and the other three blocks, Gd-DO3A-Tyr-$(C_{18})_2$, DSPE-PEG$_{2000}$-CREKA and

DSPE-PEG$_{2000}$-IR-774, were synthesized. Additionally, DSPE-PEG$_{2000}$-CERAK was synthesized as a scrambled negative control for binding assays.

2.2. Micelle preparation

Micelles were prepared by nanoprecipitation [14,15,30,31] (Fig. 1). Briefly, building blocks were dissolved in an organic mixture of acetone and ethanol (50/50 v/v) and added dropwise to ultrapure water under magnetic stirring. After 1 min, the organic phase was completely evaporated under reduced pressure over approximately 15 min, resulting in a stable and homogeneous aqueous micellar solution.

Three formulations with variable proportions of building blocks were prepared. Their molecular composition is reported in Table 2. For

Table 2
Formulations and characterization results.

Samples		Building blocks [% mol/mol]					Characterization				
		Gd-DO3A-Tyr-$(C_{18})_2$	DSPE-PEG-CREKA	DSPE-PEG-CERAK	DSPE-PEG	DSPE-PEG-IR-774	DLS		TEM [nm]	ZetaPotential [mV]	Stability [days]
							Z-average [nm]	PDI			
Mixes	Mix-1	50	20		20	10	105	0.25	10–50	−5.2	>10
	Mix-2	35	35		20	10	95	0.22	10–50	−7.4	>10
	Mix-3	20	50		20	10	117	0.37	10–100	−5.8	>10
Negative controls	Anti-Mix-1	50		20	20	10	115	0.39		−10.2	>10
	Anti-Mix-2	35		35	20	10	83	0.23		−8.8	>10
	Anti-Mix-3	20		50	20	10	98	0.29		−9.3	>10
Controls	Gd-DO3A-Tyr-$(C_{18})_2$	100					81	0.41		−23.4	<7
	DSPE-PEG-CREKA		100				286	0.55		−3.8	<7
	DSPE-PEG-CERAK			100			297	0.52		−4.3	<7
	DSPE-PEG				100		325	0.58		−4.6	>10
	DSPE-PEG-IR-774					100	140	0.45		−2.2	>10

each targeted formulation, a nontargeting (negative) control formulation was prepared by adding DSPE-PEG$_{2000}$-CERAK – a nontargeting peptide analog of CREKA.

2.3. Micelle characterization

Micelles were characterized by dynamic light scattering (DLS) in terms of their size, stability and zeta potential and by transmission electron microscopy (TEM). For these experiments, the targeted and control micelles were prepared at 1 mM (sum of the different components). The hydrodynamic diameter of the micelles was assessed by DLS, as described previously [15]. A NANO ZS ZEN 3600 instrument from Malvern (Malvern, Worcestershire, United Kingdom) controlled by ZetaSizer 7.01 software was used for particle size and zeta potential measurements. The analyses were performed with a 4 mW He–Ne laser (633 nm) at a scattering angle of 173° at 25 °C in a polystyrene semi-micro cuvette (VWR, Nyon, Switzerland). The refractive index was 1.590, and the material absorption was 0.010.

2.4. Stability

The stability of the micelles was assessed at T = 25 °C for 10 days. First, a visual inspection was performed after 7 days to evaluate aggregation, and then DLS measurements were carried out after 10 days if no aggregation was observed to confirm the visual analysis.

2.5. Transmission electron microscopy (TEM)

Mixes 1, 2 and 3 were imaged with an FEI TECNAI® G2 Sphera TEM equipped with a TCL camera (Gräfelfing, Germany). First, the samples were negatively stained with 2 % uranyl on carbon film 200-mesh copper grids. The samples were observed at 120 kV. The carbon grids were pretreated under plasma for 20 s at 0.3 Torr and 400 V.

2.6. Gadolinium (Gd) quantification

For comparison purposes and the accuracy of relaxivity calculations, the Gd-loading of the Gd-DO3A-Tyr-(C$_{18}$)$_2$ building block and the Gd-concentration in Mixes 1, 2 and 3 were precisely determined by inductively coupled plasma coupled to mass spectrometry (ICP-MS; 7800 series; Agilent, Tokyo, Japan). (Details are reported in the Sup Info.)

2.7. Nuclear magnetic resonance (NMR) relaxometry

For relaxivity measurements, mixes were prepared with a fixed concentration of Gd^{3+} of 1.0 mM. Details are reported in the Supplementary Information

Magnetic resonance imaging (MRI) phantom images and binding assay

Similar to the relaxivity measurements, the mixes and anti-mixes were prepared with a designated concentration of Gd (1, 0.5, 0.25, 0.125, 0.05 mM). Then, 200 μL of the formulations were poured into the wells of a 96-well plate. Gd-DOTA solutions at the same Gd concentrations were used as controls. Experiments were performed first without fibrin in the plates. Second, a binding assay was performed with fibrin clots, as described in the previous section (Fig. 2). Standard echo gradient 2D MRI was performed using a 3.0 T RS2D Mediso with an 8 cm core and equipped with a volume coil (excitation/reception). The MRI parameters used were coronal orientation,

12 slices × 1 mm thickness, FOV = 80 × 40 mm, TE/TR = 3.78/101 ms, matrix = 256 × 128, flip angle = 75°, 20 scans averaged, duration = 4 min 35 s. The signal intensity (SI) in the wells was quantified and normalized to noise. Regions of interest were drawn on the images using Osirix software (©Pixmeo Sarl, OsiriX Open source http://www.osirix-viewer.com). The output gave the mean and standard deviation of the signal in each well.

3. In vitro cell viability experiments

The cytotoxicity of the micelle formulations and of the building blocks alone was evaluated using a standard cell proliferation reagent (WST-1, Roche) in four different cell lines purchased from ATCC: HUVEC (human umbilical vein endothelial cells),

EC-RF24 (immortalized human vascular endothelial cells), MCF-7 (breast cancer cell line), and MCF-10 (nontumorigenic epithelial breast cell line).

Cells were grown according to ATCC guidelines at 37 °C in a humidified 5 % CO$_2$ atmosphere in appropriate medium with 10 % (v/v) heat-inactivated fetal calf serum (FCS) (Eurobio, France) and penicillin-streptomycin (10,000 U/mL) (Gibco by Life Technologies).

A total of 100 μL of cells was seeded in a 96-well plate at an initial density of 5x10^3 cells/well. After 24 h of incubation (37 °C, 5 % CO$_2$), the medium was replaced by 100 μL of a solution of mixes and controls (building blocks alone and Gd-DOTA (Dotarem®)) at different concentrations (0.1, 0.5, 1.0, 2.0, 3.0 mM) for comparison. After 24 h of incubation with the formulations, the medium was replaced by WST-1 solution according to the manufacturer's instructions (11644807001, Roche, Sigma-Aldrich, St. Gallen, Switzerland). After further incubation for 1 h at 37 °C in an incubator, the absorbance of the wells at 450 nm was read with a plate reader (Synergy 2, Biotek™) with the reference wavelength set at 690 nm, and the results were recorded with Gen5 2.00 Software. The cell viability was calculated as follows:

cell viability (%) = [(Absorbance of treated well) − (Absorbance of nontreated well)]/[(Absorbance of nontreated well) − (Absorbance of negative control)]*100.

2.8. Absorbance and fluorescence measurements

Absorbance and fluorescence were performed on the different formulations (mixes) and the fluorescent building block DSPE-PEG$_{2000}$-IR-774 alone (Sup Info Fig. SI1 and SI2).

Fluorescence binding assay of fibrin clots (Fig. 2)

The procedure for binding assays was adapted from several reports [37–39]. Fig. 2 shows the schematic representation of the assay and details are reported in the Supplementary Information.

The viability tests for each concentration were performed in triplicate.

3.1. Live-cell imaging

Intracellular localization of the micelles was performed on MCF-7 and MCF-10 cell lines. The cells were seeded at a concentration of 15,000 cells/well in a black 96-well plate (ibidi, Germany) for 3 days. Culture media were supplemented with 10 % fetal calf serum (Eurobio)
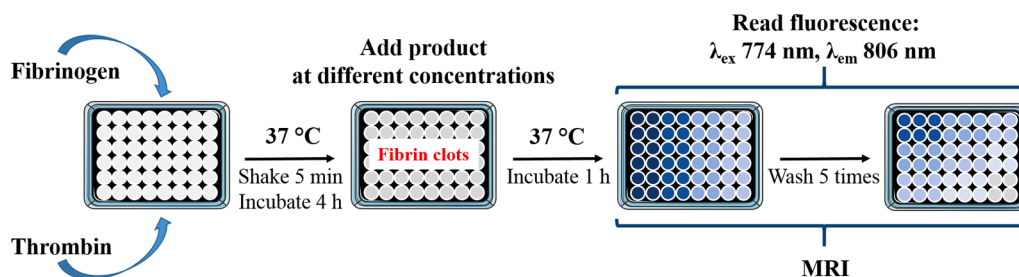
Fig. 2. Binding assay protocol.

and 1 % penicillin/streptomycin (Thermo Fisher Scientific). After 3 days, the cells were washed with PBS and incubated with fluorescent micelles at different concentrations of the dye (1, 10, 50, 100 μM) for 30 min. Mitochondria were then stained with MitoTracker® Green, and nuclei were stained with Hoechst® for 15 min. The cells were washed with PBS, incubated with Fluorobrite® medium and imaged using an IXM-XL microscope (Molecular Devices, 1x40). The images were analyzed using MetaXpress software (Molecular Devices).

3.2. Statistics

Figures and statistical analysis (2-was ANOVA test) were computed using GraphPad Prism 7.02, (GraphPad Software Inc.) software. P-values < 0.05 were considered as statistically significant.

4. Results

4.1. Synthesis of the building blocks

As described, the building blocks were synthesized according to published procedures [14,15,34–36]. The final global yield of Gd-DO3A-Tyr-$(C_{18})_2$ was 20 %, that of DSPE-PEG$_{2000}$-CREKA was 82 %, and that of DSPE-PEG$_{2000}$-IR-774 was 43 %.

4.2. Micelle mixture formulation and characterization tests

As described, micelles were formed by nanoprecipitation according to a published procedure [14,15,30,31]. Three mixes were prepared to assess the effects of different compositions on binding ability. Anti-mixes were prepared as negative controls in binding assays with a nontargeting peptide having a scrambled amino acid sequence. The characterization results are reported in Table 2. The pure building blocks were tested as well for comparison. The size of the micelles measured by DLS varied around 100 nm, as confirmed by TEM images (Fig. 3). The PDI of the micelles varied between 0.2 and 0.3, and for pure building blocks, it varied between 0.4 and 0.5. The zeta potential was slightly negative. The micelles remained stable for >10 days, with no visual precipitation or aggregation, which was confirmed by additional DLS measurements.
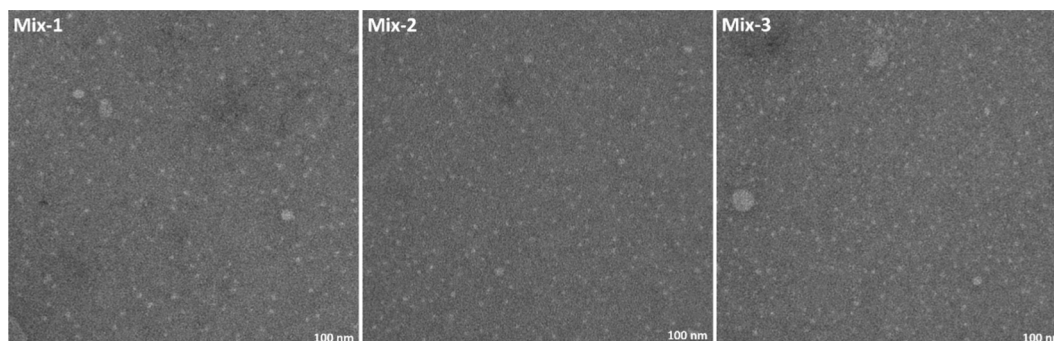
4.3. Cell cytotoxicity assay

Four different cell lines were chosen to test the toxicity of micelle mixes and the building blocks alone: two endothelial cell lines (HUVECs – human umbilical vein endothelial cells and EC-RF24 – immortalized human vascular endothelial cells) and two breast cell lines (MCF-7 – breast cancer cell line and MCF-10 – nontumorigenic epithelial breast cell line). Fig. 4 reports the results of the viability assays. The highest toxicities were observed with the nonformulated single building blocks Gd-DO3A-Tyr-$(C_{18})_2$ and DSPE-PEG$_{2000}$-IR-774. No significant toxicity, with a viability higher than 80 % at all concentrations, was observed for the mixes and anti-mixes containing the four blocks and the other two building blocks alone.

4.4. Relaxivity and MRI phantoms

To precisely calculate the relaxivity and to robustly compare with a commercial Gd-CA, the Gd loading of the chelate was first assessed by ICP-MS in the Gd-DO3A-Tyr-$(C_{18})_2$ building block. This loading was 93 %. The concentration was then adjusted to Gd^{3+} when preparing the various micelle mixes.

Fig. 5 shows the results of experiments performed with mixes at different concentrations of Gd^{3+}. Gd-DOTA was chosen as a commercial control. Fig. 5A shows MRI phantom images obtained with a 96-well plate. Fig. 5B shows the results of the relaxivity measurements determined at several magnetic fields. Fig. 5C presents signal intensity graphs, in which the values were measured from the 96-well plates shown in Fig. 5A. No visual difference was observed in Fig. 5A; however, the relaxivity of the mixes was much higher than that of Gd-DOTA (Fig. 5B), and in Fig. 5C, the signal intensities of the mixes were higher than that of Gd-DOTA.

4.5. Binding assay to fibrin clots: fluorescence measurements

The maximum spectrophotometric absorbance of the fluorescent building block was at 774 nm (Sup info Fig. SI1). Fluorescence was assessed at λ$_{ex}$ 774 nm and λ$_{em}$ 806 nm (Sup Info Fig. SI1 and SI2). Fig. 6 reports the results of the binding assay on fibrin clots. Fluorescence

Fig. 3. TEM micrographs of Mix-1, 2 and 3.
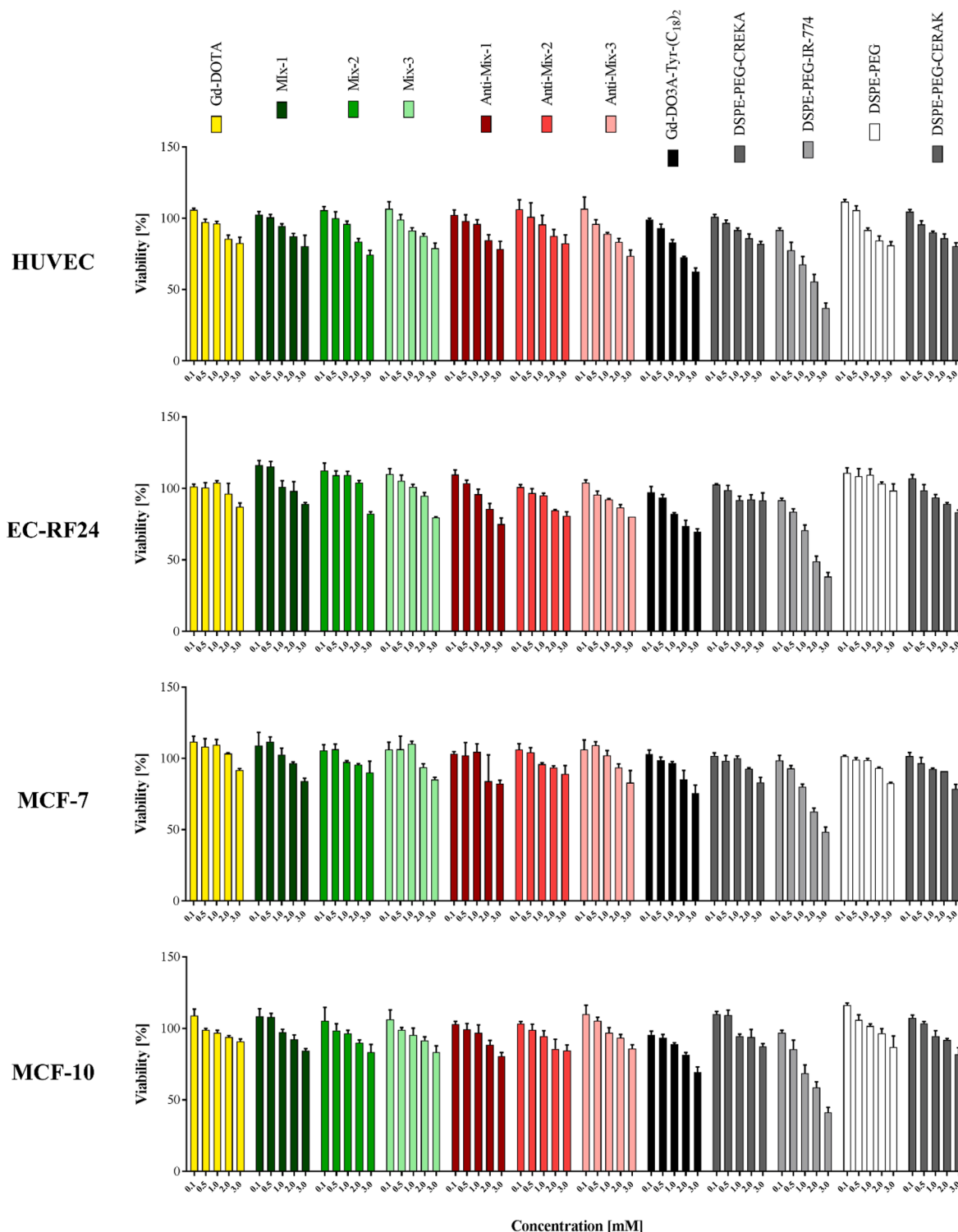
Fig. 4. Cell viability WST-1 assay in four different cell lines after 24 h of incubation: HUVECs – human umbilical vein endothelial cells, EC-RF24 – immortalized human vascular endothelial cells, MCF-7 – breast cancer cell line and MCF-10 – nontumorigenic epithelial breast cell line.

values were normalized to the dye concentration in each solution. For some solutions, overflow was observed at high concentrations; therefore, not all the solutions have experimental points up to 3 mM. Before washing, the measurements increased linearly, which is consistent with the initial dye concentration. After washing, the values for the mixes were significantly higher than those for the anti-mixes, as expected, due to the selection of the binding peptide.

Statistical analysis was performed using a 2-way ANOVA test for

each concentration between each solution. No significant difference is observed between mixes and

"All wells before washing" at $c < 1$ mM. On the opposite a significant difference is observed between mixes and anti-mixes at all tested concentrations above 0.125 mM.
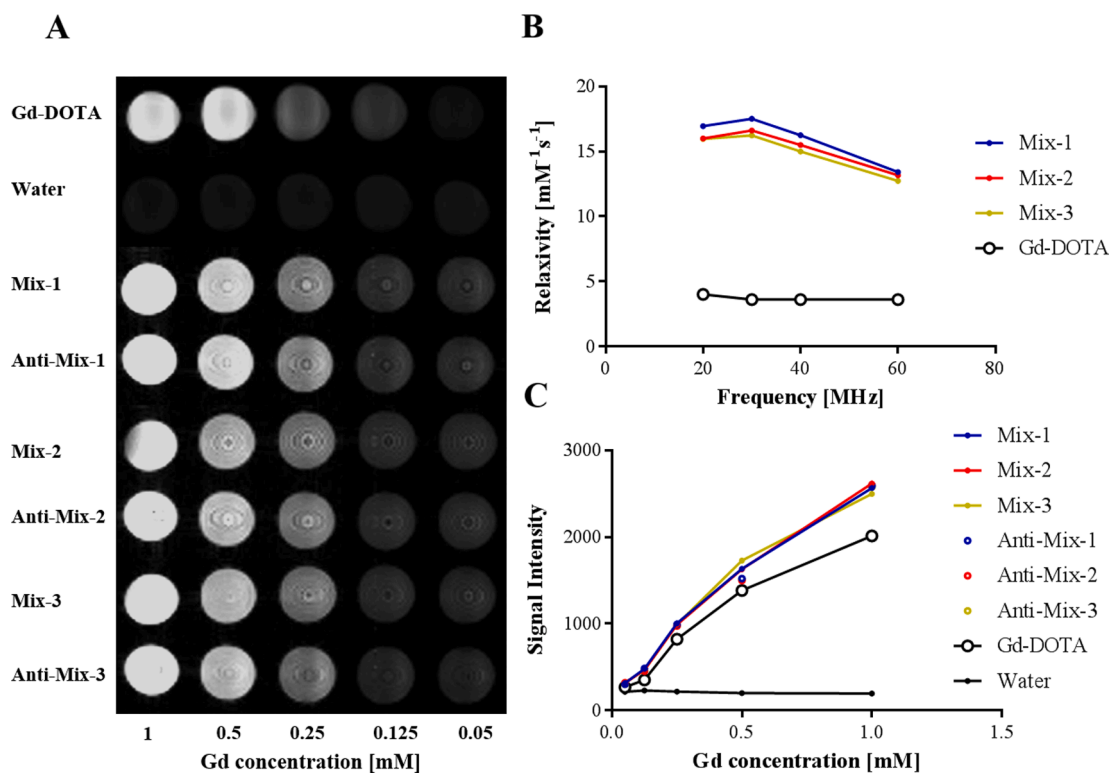
Fig. 5. A - MRI Phantoms. B - Relaxivity measurements. C - Signal intensity of MRI phantom wells.
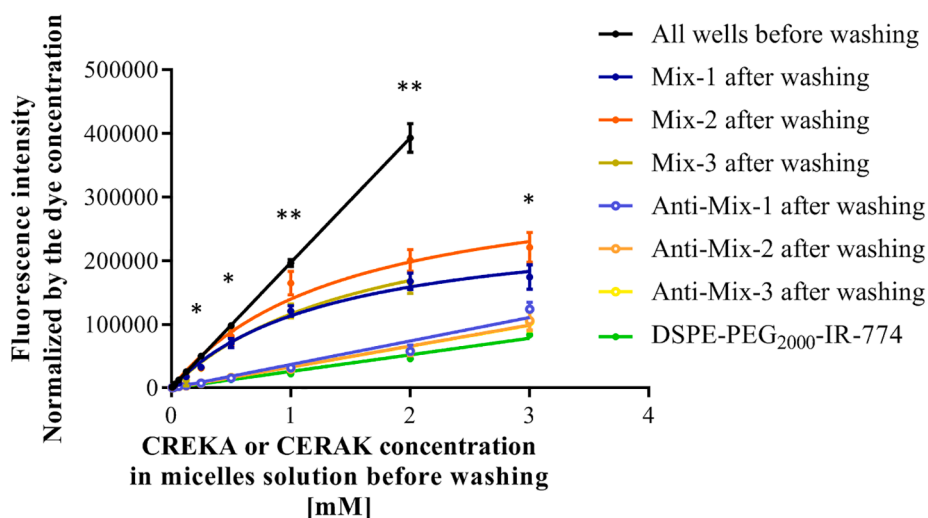

Fig. 6. Binding assay on fibrin clots: Fluorescence measurements (λ_{ex} 774 nm, λ_{em} 806 nm) before and after 5 washes. *Significant difference (0.05) between mixes and anti-mixes. **Significant difference (0.05) between mixes, anti-mixes and "All wells before washing".

*4.6. Binding assay to fibrin clots: MR imaging*

A binding assay was also performed by MRI in 96-well plates with fibrin-coated wells. For this experiment, the molecular concentration of building blocks in the micelles was adjusted to that of Gd^{3+}. Fig. 7A shows the MRI of the phantom with images of the plates before and after washing. Fig. 7B presents the signal intensities on the phantoms. A steady increase in the signal as a function of Gd^{3+} concentration was observed in all wells before washing. After plate washing, the signal intensities of the targeted mixes were in all cases higher than those of the anti-mixes. In the case of Gd-DOTA, the signal was very low. This was expected, as this complex cannot bind to fibrin.

Statistical analysis was performed using a 2-way ANOVA test for each concentration between each solution. No significant difference is observed between solutions at c < 0.25 mM. Further, a significant difference is observed between "All wells before washing", mixes and anti-mixes starting from c = 0.25 mM, and as well between anti-mixes and Gd-DOTA starting from c = 0.5 mM.

4.7. Cell fluorescence imaging

Cell internalization and fluorescence imaging were performed on MCF-7 and MCF-10 cells. Tests were performed on mixes and anti-mixes. Images of selected cells for Mix-1 and Anti-Mix-1 are presented in Fig. 8; the images of the other mixes and anti-mixes and the resulting fluorescence graph are in the Supplementary Information (Fig. SI4 and SI5).
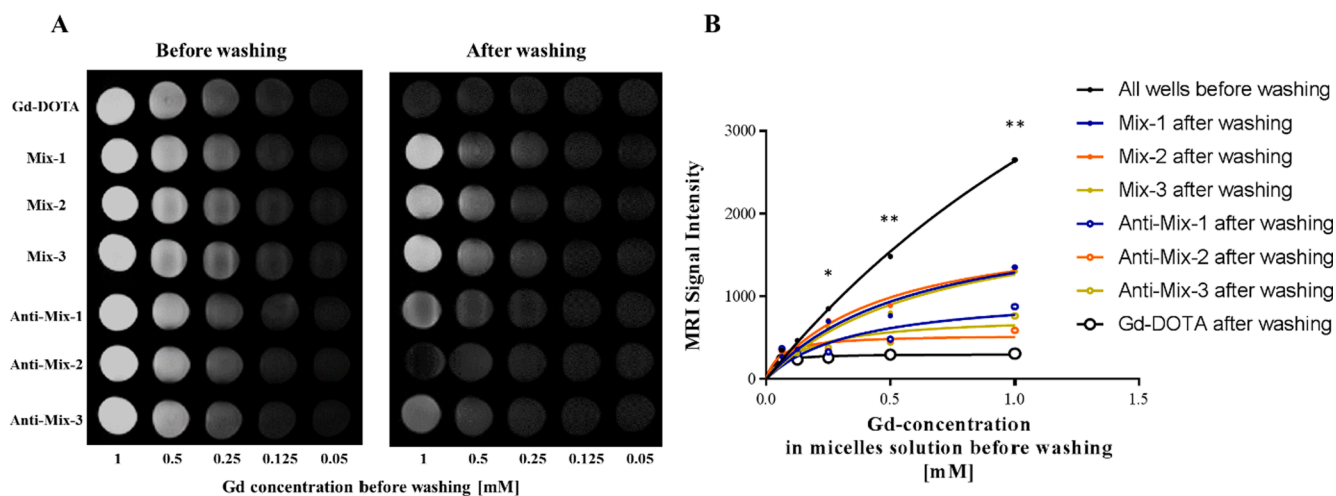
Fig. 7. Binding assay on fibrin clots. A – MRI of the wells before and after washing. B – MRI signal intensity of the wells as a function of Gd concentration. *Significant difference (0.05) between "All wells before washing", mixes and anti-mixes. ** Significant difference (0.05) between "All wells before washing", mixes, anti-mixes and Gd-DOTA.
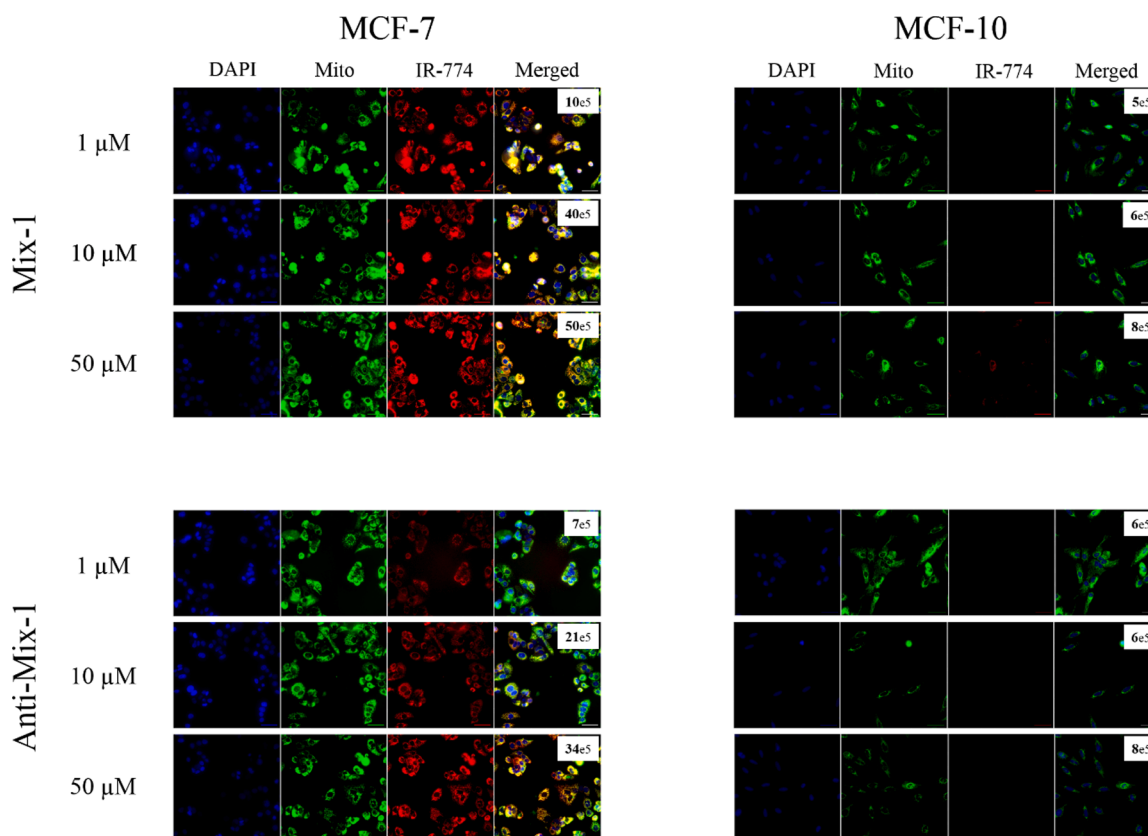
Fig. 8. Cell fluorescence imaging for Mix-1 and Anti-Mix-1 on MCF-7 and MCF-10 cell lines (scale bar = 50 μm). In the upper right corner for each concentration, the fluorescence integrated intensity of the whole well is indicated.

Internalization was observed for MCF-7 cells at practically all concentrations. In contrast, this was only slightly observed at 50 μM in MCF-10 cells.

5. Discussion

5.1. Micelle formulations

Micelle formulations were chosen for this study. Micelles bear several advantages relative to other types of nanoconstructs. First, they are simple to formulate by using the nanoprecipitation technique. Second, we have already used this formulation method and proved its robustness and repeatability to provide an MRI blood pool contrast agent [15,31]. Third, in the present study, the micelles obtained were homogeneous with regard to their size in all mixes (Table 2), as confirmed on TEM micrographs (Fig. 3). It has been shown that it is important to have building blocks with both a hydrophilic and hydrophobic tail to obtain a narrow size distribution of the micelles [40,41].

The building blocks alone also form supramolecular constructs but have a larger size distribution and a higher PDI. Interestingly, variation of the molar ratio of the Gd building block to peptide-bearing building block did not greatly influence the size. However, Mix-2 had the lowest size (95 nm) and the lowest PDI (0.22), which is also the case for Anti-Mix-2. Finally, the size range obtained, between 10 and 100 nm, is exactly the one needed for prolonged blood circulation [42]. With this mean size, the micelles are not prone to massive vascular extravasation and excessively fast renal excretion.

5.2. Building block choice

Four building blocks were selected for the mixed micelles. Each block has a specific role (Table 1) and was carefully chosen to formulate target-specific micelles, enabling vascular molecular imaging.

Gd-DO3A-Tyr-$(C_{18})_2$ is responsible for MRI contrast; it has a DOTA-based ligand loaded with a Gd^{3+} cation and two lipophilic arms. Gd-DOTA chelate has been proven to be more stable than Gd-DTPA in several media, with almost no Gd release *in vivo* [32,43]. Additionally, this building block includes two C_{18} chains, which participate in the hydrophobic core of the micelles.

DSPE-PEG$_{2000}$-CREKA is responsible for the binding properties. As described above, cardiovascular-related diseases, frequently involving unstable plaques containing a soft atheromatous core, are a major cause of disability and death; therefore, early imaging is the key to the close-up monitoring of the evolution and treatment of this cardiovascular disorder. Unstable and partially ruptured plaques develop fibrin clots. The CREKA pentapeptide was chosen as the targeting moiety since this short peptide specifically binds to fibrin clots. Moreover, CREKA-targeted CAs have been successfully tested in cancer imaging [18,38,44].

DSPE-PEG$_{2000}$-IR-774 was synthesized and used in this study for the orthogonal detection of micelles by fluorescence imaging. This fluorescent near-infrared-emitting dye does not influence the micelle structure and was first developed in our lab for specific cancer cell internalization. It could add multimodality in these micelles for cancer imaging.

Finally, DSPE-PEG$_{2000}$ possesses the hydrophobic and hydrophilic chains responsible for the micelle core structure. The PEG$_{2000}$ chains provide long blood circulation and stealth properties to micelles, and DSPE molecules contribute to the consolidation of the whole structure.

As discussed above, the lowest PDI was observed in the different mixes and not in the building blocks alone, which are assembled as molecule aggregates rather than micelles. This was also demonstrated by the stability assay (Table 2).

5.3. Mix characterizations

The mixed-micelle strategy, using several different building blocks, was chosen as the formulation technique to help overcome liver accumulation. Most often, micelles with one building block are very stable, and some of them are trapped by the liver for a prolonged period of time, which is not a viable approach. On the other side mixed-micelles will decompose faster and expectantly will be eliminated with no liver accumulation.

Three mix compositions were chosen (Table 2) to test the influence of different building blocks. DSPE-PEG$_{2000}$ and DSPE-PEG$_{2000}$-IR-774 had their molar fraction fixed, and Gd-DO3A-Tyr-$(C_{18})_2$ and DSPE-PEG$_{2000}$-CREKA were included at various proportions between 20 % and 50 %. For each experiment, the concentration of a specific building block was fixed to a value to allow comparison.

Several characterization assays were performed. The first was the cell viability assay. One breast cancer cell line, one healthy breast cell line and two vascular cell lines were tested. As shown in Fig. 4, no significant cytotoxicity was observed for the mixes and anti-mixes, demonstrating the suitability of the mixture of components in the micelles. Interestingly, building blocks DSPE-PEG$_{2000}$-IR-774 and Gd-DO3A-Tyr-$(C_{18})_2$ were more toxic when tested by themselves but only at concentrations that would never be reached *in vivo*.

Another important measurement was the relaxivity determination of the developed CA. In Fig. 5B, the relaxivity graph shows a curve for the three mixes, proving the formation of a nanostructure in solution. Moreover, the relaxivity of the micelles was much higher than that of the marketed Gd-DOTA. This property is very important with high-field magnets, as has already been discussed in our previous works [14,15,31].

This assay is used in conjunction with MRI phantom imaging and signal intensity measurements. In Fig. 5A, no visual difference was observed between the mixes, anti-mixes and marketed Gd-DOTA. However, in the SI graphs, the intensities for the mixes and anti-mixes were slightly higher than those of Gd-DOTA. The concentration of Gd in the mixes was precisely measured by ICP-MS; therefore, this difference is less likely due to the Gd concentration. Consequently, this difference can be clearly attributed to the difference in relaxivity.

In short, mixed micelles formulated with sizes ranging from 10 to 100 nm are suitable for applications where blood circulation and vascular targeting rather than diffusion in tissues is desired. They showed no toxicity toward different cell lines, particularly vascular cell lines. Finally, they have a high relaxivity, which makes them visible on MRI even at low concentrations.

5.4. Binding properties

The most important assay for these formulations was the binding assay. The goal of this work was to formulate a CA with strong binding properties to fibrin clots. We wanted to first determine the binding potential and then the best mix composition, as we have several building blocks.

Two orthogonal binding assays on fibrin clots were performed. One was a fluorescence detection method, and the other was MRI imaging and SI quantification.

For the fluorescence assay, anti-mixes were used as the nontargeted controls, and DSPE-PEG$_{2000}$-IR-774 was used as the negative control. The results are reported in Fig. 6. The mixes resulted in curves proving the specific binding with a saturation of binding sites. Mix-2 seems to have a higher binding property. The anti-mixes and the dye alone resulted in a straight line, demonstrating unspecific binding, which was much lower than that of the mixes. Statistically a significant difference ($p < 0.05$) is observed between mixes and anti-mixes at almost at all concentrations, and between mixes and the wells before washing starting at c = 1 mM.

The MRI assay provided corresponding results. Fig. 7A shows that mixes remain attached to fibrin clots more than the anti-mixes do. Here, the negative control was Gd-DOTA, which was completely washed and had no binding affinity at all due to its small size. The SI graph confirms the visual analysis. The curve of the mixes was always higher, and the anti-mixes gave rise to a straight line. Interestingly, no difference was observed between the mixes. Here as well the significant difference is statistically proved ($p < 0.05$) between mixes, anti-mixes and the "wells before washing" starting from c = 0.25 mM.

Therefore, the binding property was clearly demonstrated with these two assays.

All three mixes were attached to fibrin clots, and Mix-2 seems to have better binding properties. Furthermore, nontargeted and negative controls support the conclusion.

5.5. Internalization properties

Micelles have been designed to first target fibrin clots for atheroma MRI imaging.

In addition, the fluorescent dye used for orthogonal detection in the binding assays was designed in our laboratory to target cancer cells. This property was tested for all micelles in an additional cell internalization assay to show their potential application in cancer cell detection. The fluorescent dye is positively charged (Tables 1 and 2) and therefore accumulates preferentially in the mitochondria of cancer cells rather than in healthy cells due to the higher mitochondrial membrane potential of cancer cells [45]. The cell internalization of the fluorescent micelles was therefore tested in cancer and healthy cell lines by measuring the colocalization of the fluorescent dye and a MitoTracker™ using confocal imaging. As shown in Fig. 8, the micelles effectively enter cancer cells at much lower concentrations (1–10 μM) than they enter into the healthy cell line (10–50 μM). Additionally, it seems that Mix-1 enters the cells better than Anti-Mix-1, since CREKA aids in entering cancer cells [46,47]. However, this difference is not obvious, and CREKA will attach the CAs to the cancer tumor by targeting the leaking vessels, and then DSPE-PEG$_{2000}$-IR-774 enables cancer cell entry.

For the three mixes and anti-mixes, internalization was observed at 10 μM in the

MCF-7 cancer cells (Sup Info Fig. SI3). In contrast, for MCF-10 healthy cells, internalization was barely observed at 50 μM (Sup Info Fig. SI4).

The fluorescence quantification graph (Sup Info Fig. SI5) confirms the visual result and shows a small difference between the mixes and anti-mixes in terms of cancer cell line internalization. This strongly suggests that CREKA improves cell internalization. Notably, this difference was not observed in healthy cells. This is due to the high expression of fibronectin in the microenvironment of tumor and especially in high-risk metastasis breast tumors. The mortality of breast cancer is mostly due to metastases formation in other organs such as lungs [48,49]. Therefore, the early diagnosis of high-risk metastases mammary tumors is crucial for the success of anticancer treatment. It has been shown that the evolution of a tumor into metastases can be detected early at the molecular level [50]. In fact, the metastases formation is driven by a process called epithelial to mesenchymal transition (EMT) [51,52]. EMT is characterized by molecular events such as the upregulation of fibronectin [53–56]. CREKA can be used to target fibronectin highly expressed in metastases and improve the survival rate of breast cancer.

These results show the potential use of our micelles for the detection of cancer cells by fluorescence imaging. Multifunctionality in imaging fibrin clots, on the one hand, and cancer cells, on the other hand, would be a desirable property for a new CA. This additional assay supports this possibility; however, additional studies still have to be performed.

5.6. Comparison to similar CREKA nanoconstructs and perspectives

Recently, several groups have been working on CREKA-based nanostructures [18,28,36,38,39,44,57–59]. The potential of this pentapeptide to bind fibrin-fibronectin complexes has been proven and tested with several products for different indications [18,28,46,60,61]. Groups have developed products for imaging cancer and atheroma with promising results.

Cancer imaging requires a smaller structure, which can rapidly exit vessels and rapidly reach the target. Several research groups have reported new molecules attaching several Gd-DOTA rings [28,57]. In another study, CREKA was bound to PAMAM dendrimer nanoparticles,

and they were tested on glioblastomas [44]. They integrated an infrared dye to achieve multimodality imaging. A micelle structure similar to ours has been developed for imaging atherosclerotic lesions [36]; however, the authors used a Gd-DTPA chelate instead of Gd-DO3A and did not test cancer cell targeting.

Our micelles perfectly integrate the family of CREKA structures with potential for atheroma and cancer imaging. Size homogeneity and stability are in hand with future *in vivo* trials. Nontoxicity and high relaxivity are also important characteristics for MRI CAs. Three mixes were tested, and Mix-2 seems to have several advantages compared to the others, particularly in the fluorescence binding assay.

5.7. General conclusion

To summarize, our micelles have high potential as multimodal MRI CAs for atheroma and most likely cancer imaging. The building blocks are simple to synthesize, and the nanoprecipitation formulation method has proven its benefit. Binding assays proved the hypothesis of possible targeted molecular imaging. The next step will be *in vivo* trials on several mouse models.

Declaration of Competing Interest

The authors declare that they have no known competing financial interests or personal relationships that could have appeared to influence the work reported in this paper.

Appendix A. Supplementary material

Supplementary data to this article can be found online at https://doi.org/10.1016/j.ejpb.2020.11.017.

References

[1] H. Wang, M. Naghavi, C. Allen, et al., Global, regional, and national life expectancy, all-cause mortality, and cause-specific mortality for 249 causes of death, 1980–2015: a systematic analysis for the Global Burden of Disease Study 2015, The Lancet 388 (10053) (2016) 1459–1544.

[2] M.L. Lord, D.R. Chettle, J.L. Gräfe, M.D. Noseworthy, F.E. McNeill, Observed Deposition of gadolinium in bone using a new noninvasive in vivo biomedical device: results of a small pilot feasibility study, Radiology 287 (1) (2018) 96–103.

[3] J. Vymazal, E. Spuentrup, G. Cardenas-Molina, A.J. Wiethoff, M.G. Hartmann, P. Caravan, E.C. Parsons Jr, Thrombus imaging with fibrin-specific gadolinium-based MR contrast agent EP-2104R: results of a phase II clinical study of feasibility, Invest. Radiol. 44 (11) (2009) 697–704.

[4] C. Zhang, M. Jugold, E.C. Woenne, T. Lammers, B. Morgenstern, M.M. Mueller, H. Zentgraf, M. Bock, M. Eisenhut, W. Semmler, F. Kiessling, Specific targeting of tumor angiogenesis by RGD-conjugated ultrasmall superparamagnetic iron oxide particles using a clinical 1.5-T magnetic resonance scanner, Cancer Res. 67 (4) (2007) 1555–1562.

[5] R.B. Lauffer, Paramagnetic metal complexes as water proton relaxation agents for NMR imaging: theory and design, Chem. Rev. 87 (5) (1987) 901–927.

[6] P. Caravan, J.J. Ellison, T.J. McMurry, R.B. Lauffer, Gadolinium(III) chelates as MRI contrast agents: structure, dynamics, and applications, Chem. Rev. 99 (9) (1999) 2293–2352.

[7] E.A. Tanifum, C. Patel, M.E. Liaw, R.G. Pautler, A.V. Annapragada, Hydrophilic fluorinated molecules for spectral 19F MRI, Sci. Rep. 8 (1) (2018), https://doi.org/10.1038/s41598-018-21178-3.

[8] Dominique Meyer, Michel Schaefer, Bruno Bonnemain, Gd-DOTA, a potential MRI contrast agent current status of physicochemical knowledge, Invest. Radiol. 23 (1988) S232–S235.

[9] D.H. Carr, J. Brown, G.M. Bydder, R.E. Steiner, H.J. Weinmann, U. Speck, A.S. Hall, I.R. Young, Gadolinium-DTPA as a contrast agent in MRI: initial clinical experience in 20 patients, Am. J. Roentgenol. 143 (2) (1984) 215–224.

[10] P. Marckmann, L. Skov, K. Rossen, A. Dupont, M.B. Damholt, J.G. Heaf, H. S. Thomsen, Nephrogenic systemic fibrosis: suspected causative role of gadodiamide used for contrast-enhanced magnetic resonance imaging, JASN 17 (9) (2006) 2359–2362.

[11] T. Kanda, T. Fukusato, M. Matsuda, K. Toyoda, H. Oba, J. Kotoku, T. Haruyama, K. Kitajima, S. Furui, Gadolinium-based contrast agent accumulates in the brain even in subjects without severe renal dysfunction: evaluation of autopsy brain specimens with inductively coupled plasma mass spectroscopy, Radiology 276 (1) (2015) 228–232.

[12] M.F. Tweedle, S.M. Eaton, W.C. Eckelman, et al., Comparative chemical structure and pharmacokinetics of MRI contrast agents, Invest. Radiol. 23 (1988) S236–S239.

[13] C. Klessen, P.A. Hein, A. Huppertz, M. Voth, M. Wagner, T. Elgeti, H. Kroll, B. Hamm, M. Taupitz, P. Asbach, First-pass whole-body magnetic resonance angiography (MRA) using the blood-pool contrast medium gadofosveset trisodium: comparison to gadopentetate dimeglumine, Invest. Radiol. 42 (9) (2007) 659–664.

[14] A. Babič, V. Vorobiev, G. Trefalt, L.A. Crowe, L. Helm, J.-P. Vallée, E. Allémann, MRI micelles self-assembled from synthetic gadolinium-based nano building blocks, Chem. Commun. 55 (7) (2019) 945–948, https://doi.org/10.1039/c8cc08875f.

[15] V. Vorobiev, A. Babič, L.A. Crowe, Y. Van De Looij, S. Lenglet, A. Thomas, L. Helm, J.-P. Vallée, E. Allémann, Pharmacokinetics and biodistribution study of self-assembled Gd-micelles demonstrating blood-pool contrast enhancement for MRI, Int. J. Pharm. 568 (2019) 118496, https://doi.org/10.1016/j.ijpharm.2019.118496.

[16] M.D. Ogan, U. Schmiedl, M.E. Moseley, W. Grodd, H. Paajanen, R.C. Brasch, Albumin labeled with Gd-DTPA: an intravascular contrast-enhancing agent for magnetic resonance blood pool imaging: preparation and characterization, Invest. Radiol. 22 (8) (1987) 665–671.

[17] S.S. Ahn, M.-J. Kim, J.S. Lim, H.-S. Hong, Y.E. Chung, J.-Y. Choi, Added value of gadoxetic acid–enhanced hepatobiliary phase MR imaging in the diagnosis of hepatocellular carcinoma, Radiology 255 (2) (2010) 459–466.

[18] B.o. Zhang, H. Wang, S. Shen, X. She, W. Shi, J. Chen, Q. Zhang, Y.u. Hu, Z. Pang, X. Jiang, Fibrin-targeting peptide CREKA-conjugated multi-walled carbon nanotubes for self-amplified photothermal therapy of tumor, Biomaterials 79 (2016) 46–55.

[19] E. Werner, A. Datta, C. Jocher, K. Raymond, High-relaxivity MRI contrast agents: where coordination chemistry meets medical imaging, Angew. Chem. Int. Ed. 47 (45) (2008) 8568–8580.

[20] P. Caravan, Strategies for increasing the sensitivity of gadolinium based MRI contrast agents, Chem. Soc. Rev. 35 (6) (2006) 512, https://doi.org/10.1039/b510982p.

[21] A.J. L. Villaraza, A. Bumb, M.W. Brechbiel, Macromolecules, dendrimers, and nanomaterials in magnetic resonance imaging: the interplay between size, function, and pharmacokinetics, Chem. Rev. 110 (5) (2010) 2921–2959.

[22] H.B. Na, I.C. Song, T. Hyeon, Inorganic nanoparticles for MRI contrast agents, Adv. Mater. 21 (21) (2009) 2133–2148.

[23] H. Kobayashi, M.W. Brechbiel, Dendrimer-based nanosized MRI contrast agents, Curr. Pharm. Biotechnol. 5 (6) (2004) 539–549.

[24] E. Spuentrup, R.M. Botnar, A.J. Wiethoff, T. Ibrahim, S. Kelle, M. Katoh, M. Özgun, E. Nagel, J. Vymazal, P.B. Graham, R.W. Günther, D. Maintz, MR imaging of thrombi using EP-2104R, a fibrin-specific contrast agent: initial results in patients, Eur. Radiol. 18 (9) (2008) 1995–2005.

[25] R.B. Lauffer, D.J. Parmelee, S.U. Dunham, H.S. Ouellet, R.P. Dolan, S. Witte, T. J. McMurry, R.C. Walovitch, MS-325: albumin-targeted contrast agent for MR angiography. Radiology 207 (2) (1998) 529–538.

[26] P. Caravan, B. Das, S. Dumas, F. Epstein, P. Helm, V. Jacques, S. Koerner, A. Kolodziej, L. Shen, W.-C. Sun, Z. Zhang, Collagen-targeted MRI contrast agent for molecular imaging of fibrosis, Angew. Chem. Int. Ed. 46 (43) (2007) 8171–8173.

[27] M.K. Islam, S. Kim, H.-K. Kim, S. Park, G.-H. Lee, H.J. Kang, J.-C. Jung, J.-S. Park, T.-J. Kim, Y. Chang, Manganese complex of ethylenediaminetetraacetic acid (EDTA)–benzothiazole aniline (BTA) conjugate as a potential liver-targeting MRI contrast agent, J. Med. Chem. 60 (7) (2017) 2993–3001.

[28] Z. Zhou, M. Qutaish, Z. Han, R.M. Schur, Y. Liu, D.L. Wilson, Z.-R. Lu, MRI detection of breast cancer micrometastases with a fibronectin-targeting contrast agent, Nat. Commun. 6 (1) (2015), https://doi.org/10.1038/ncomms8984.

[29] R.L. Reddick, S.H. Zhang, N. Maeda, Atherosclerosis in mice lacking apo E. Evaluation of lesional development and progression. Arterioscler. Thromb. 14 (1) (1994) 141–147.

[30] S. Adriouach, V. Vorobiev, G. Trefalt, E. Allémann, N. Lange, A. Babič, Squalene-PEG: Pyropheophorbide-a nanoconstructs for tumor theranostics, Nanomed. Nanotechnol. Biol. Med. 15 (1) (2019) 243–251, https://doi.org/10.1016/j.nano.2018.09.013.

[31] A. Babič, V. Vorobiev, C. Xayaphoummine, G. Lapicorey, A.-S. Chauvin, L. Helm, E. Allémann, Self-assembled nanomicelles as MRI blood-pool contrast agent, Chem. Eur. J. 24 (6) (2018) 1348–1357, https://doi.org/10.1002/chem.201703962.

[32] K. Nwe, M. Bernardo, C.A.S. Regino, M. Williams, M.W. Brechbiel, Comparison of MRI properties between derivatized DTPA and DOTA gadolinium–dendrimer conjugates, Bioorg. Med. Chem. 18 (16) (2010) 5925–5931.

[33] B. Ashok, L. Arleth, R.P. Hjelm, I. Rubinstein, H. Önyüksel, In vitro characterization of PEGylated phospholipid micelles for improved drug solubilization: effects of PEG chain length and PC incorporation, J. Pharm. Sci. 93 (10) (2004) 2476–2487.

[34] I. Noh, D. Lee, H. Kim, C.-U. Jeong, Y. Lee, J.-O. Ahn, H. Hyun, J.-H. Park, Y.-C. Kim, Enhanced photodynamic cancer treatment by mitochondria-targeting and brominated near-infrared fluorophores, Adv. Sci. 5 (3) (2018) 1700481, https://doi.org/10.1002/advs.v5.310.1002/advs.201700481.

[35] J.D. Routledge, M.W. Jones, S. Faulkner, M. Tropiano, Kinetically stable lanthanide complexes displaying exceptionally high quantum yields upon long-wavelength excitation: synthesis, photophysical properties, and solution speciation, Inorg. Chem. 54 (7) (2015) 3337–3345.

[36] S.P. Yoo, F. Pineda, J.C. Barrett, C. Poon, M. Tirrell, E.J. Chung, Gadolinium-functionalized peptide amphiphile micelles for multimodal imaging of atherosclerotic lesions, ACS Omega 1 (5) (2016) 996–1003.

[37] A.M. Kruse, S.A. Meenach, K.W. Anderson, J.Z. Hilt, Synthesis and characterization of CREKA-conjugated iron oxide nanoparticles for hyperthermia applications, Acta Biomater. 10 (6) (2014) 2622–2629.

[38] A.C. Okur, P. Erkoc, S. Kizilel, Targeting cancer cells via tumor-homing peptide CREKA functional PEG nanoparticles, Colloids Surf., B 147 (2016) 191–200.

[39] Y. Zhang, L. Wang, S. Yu, K. Hu, S. Huang, Y. Li, H. Wu, H. Li, Q. Wang, Synthesis and preclinical evaluation of the fibrin-binding cyclic peptide 18 F-iCREKA: comparison with its contrasted linear peptide, Contrast Media Mol. Imag. 2019 (2019) 1–11.

[40] D.L. Wise, D.J. Trantolo, Process Engineering for Pollution Control and Waste Minimization, M. Dekker, New York, 1994.

[41] Y. Einaga, A.i. Kusumoto, A. Noda, Effects of hydrophobic chain length on the micelles of heptaoxyethylene hexadecyl C16E7 and octadecyl C18E7 ethers, Polym. J. 37 (5) (2005) 368–375.

[42] M. Longmire, P.L. Choyke, H. Kobayashi, Clearance properties of nano-sized particles and molecules as imaging agents: considerations and caveats, Nanomedicine 3 (5) (2008) 703–717.

[43] M. Magerstädt, O.A. Gansow, M.W. Brechbiel, D. Colcher, L. Baltzer, R.H. Knop, M. E. Girton, M. Naegele, Gd(DOTA): An alternative to Gd(DTPA) as aT1,2 relaxation agent for NMR imaging or spectroscopy, Magn. Reson. Med. 3 (5) (1986) 808–812.

[44] J. Zhao, B.o. Zhang, S. Shen, J. Chen, Q. Zhang, X. Jiang, Z. Pang, CREKA peptide-conjugated dendrimer nanoparticles for glioblastoma multiforme delivery, J. Colloid Interface Sci. 450 (2015) 396–403.

[45] S. Fulda, L. Galluzzi, G. Kroemer, Targeting mitochondria for cancer therapy, Nat. Rev. Drug Discov. 9 (6) (2010) 447–464.

[46] E.J. Chung, Y.u. Cheng, R. Morshed, K. Nord, Y.u. Han, M.L. Wegscheid, B. Auffinger, D.A. Wainwright, M.S. Lesniak, M.V. Tirrell, Fibrin-binding, peptide amphiphile micelles for targeting glioblastoma, Biomaterials 35 (4) (2014) 1249–1256.

[47] D. Simberg, T. Duza, J.H. Park, M. Essler, J. Pilch, L. Zhang, A.M. Derfus, M. Yang, R.M. Hoffman, S. Bhatia, M.J. Sailor, E. Ruoslahti, Biomimetic amplification of nanoparticle homing to tumors, PNAS 104 (3) (2007) 932–936.

[48] G. Uzunalli, A.M. Dieterly, C.M. Kemet, H.-Y. Weng, A.H. Soepriatna, C.J. Goergen, A.B. Shinde, M.K. Wendt, L.T. Lyle, Dynamic transition of the blood-brain barrier in the development of non-small cell lung cancer brain metastases, Oncotarget 10 (59) (2019) 6334–6348.

[49] A. Shinde, T. Wilmanski, H. Chen, D. Teegarden, M.K. Wendt, Pyruvate carboxylase supports the pulmonary tropism of metastatic breast cancer, Breast Cancer Res. 20 (1) (2018), https://doi.org/10.1186/s13058-018-1008-9.

[50] A. Shinde, J.S. Paez, S. Libring, K. Hopkins, L. Solorio, M.K. Wendt, Transglutaminase-2 facilitates extracellular vesicle-mediated establishment of the metastatic niche, Oncogenesis 9 (2) (2020), https://doi.org/10.1038/s41389-020-0204-5.

[51] S.D. Hardy, A. Shinde, W.-H. Wang, M.K. Wendt, R.L. Geahlen, Regulation of epithelial-mesenchymal transition and metastasis by TGF-β, P-bodies, and autophagy, Oncotarget 8 (61) (2017) 103302–103314.

[52] A. Shinde, S.D. Hardy, D. Kim, S.S. Akhand, M.K. Jolly, W.-H. Wang, J.C. Anderson, R.B. Khodadadi, W.S. Brown, J.T. George, S. Liu, J. Wan, H. Levine, C.D. Willey, C. J. Krusemark, R.L. Geahlen, M.K. Wendt, Spleen tyrosine kinase–mediated autophagy is required for epithelial–mesenchymal plasticity and metastasis in breast cancer, Cancer Res. 79 (8) (2019) 1831–1843.

[53] B.H. Jun, T. Guo, S. Libring, et al., Fibronectin-expressing mesenchymal tumor cells promote breast cancer metastasis, Cancers (Basel) 12 (9) (2020).

[54] A. Shinde, S. Libring, A. Alpsoy, A. Abdullah, J.A. Schaber, L. Solorio, M.K. Wendt, Autocrine fibronectin inhibits breast cancer metastasis, Mol. Cancer Res. 16 (10) (2018) 1579–1589.

[55] T. Wilmanski, X. Zhou, W. Zheng, A. Shinde, S.S. Donkin, M. Wendt, J.R. Burgess, D. Teegarden, Inhibition of pyruvate carboxylase by 1α,25-dihydroxyvitamin D promotes oxidative stress in early breast cancer progression, Cancer Lett. 411 (2017) 171–181.

[56] S. Libring, A. Shinde, M.K. Chanda, et al., The dynamic relationship of breast cancer cells and fibroblasts in fibronectin accumulation at primary and metastatic tumor sites, Cancers 12 (5) (2020) 1270.

[57] X. Wu, G. Yu, D. Lindner, S.M. Brady-Kalnay, Q. Zhang, Z.R. Lu, Peptide targeted high-resolution molecular imaging of prostate cancer with MRI, Am. J. Nucl. Med. Mol. Imaging 4 (6) (2014) 525–536.

[58] Y. Song, Z. Huang, J. Xu, D. Ren, Y.u. Wang, X. Zheng, Y. Shen, L. Wang, H. Gao, J. Hou, Z. Pang, J. Qian, J. Ge, Multimodal SPION-CREKA peptide based agents for molecular imaging of microthrombus in a rat myocardial ischemia-reperfusion model, Biomaterials 35 (9) (2014) 2961–2970.

[59] D. Peters, M. Kastantin, V.R. Kotamraju, P.P. Karmali, K. Gujraty, M. Tirrell, E. Ruoslahti, Targeting atherosclerosis by using modular, multifunctional micelles, Proc. Natl. Acad. Sci. 106 (24) (2009) 9815–9819.

[60] Z. Zhou, X. Wu, A. Kresak, M. Griswold, Z.-R. Lu, Peptide targeted tripod macrocyclic Gd(III) chelates for cancer molecular MRI, Biomaterials 34 (31) (2013) 7683–7693.

[61] J. Hamzah, V.R. Kotamraju, J.W. Seo, L. Agemy, V. Fogal, L.M. Mahakian, D. Peters, L. Roth, M.K.J. Gagnon, K.W. Ferrara, E. Ruoslahti, Specific penetration and accumulation of a homing peptide within atherosclerotic plaques of apolipoprotein E-deficient mice, Proc. Natl. Acad. Sci. 108 (17) (2011) 7154–7159.